ISSN 1054-660X, Laser Physics, 2007, Vol. 17, No. 5, pp. 608–617.

Control of Cluster Multielectron Ionization in Ultraintense Laser Fields

A. Heidenreich, I. Last, and J. Jortner*

School of Chemistry, Tel Aviv University, Tel Aviv, 69978 Israel

*e-mail: jortner@chemsg1.tau.ac.il

Received November 14, 2006

Abstract—We performed classical molecular dynamics simulations to explore the controllability of the inner ionization process in Xe_n clusters (n = 2–2171), driven by ultraintense infrared Gaussian laser fields (peak intensity $I_M = 10^{15}$–10^{18} W cm^{-2}, temporal pulse length τ = 10–100 fs, and frequency ν = 0.35 fs^{-1}). Controllability of ion charge abundances and of their spatial distributions inside the cluster emerges from the different pulse length dependences of classical barrier suppression ionization (BSI) and of electron impact ionizations (EII), as well as from the time scale of the Coulomb explosion (CE). For large clusters (Xe_{2171}), low intensities (10^{15} W cm^{-2}), and long pulses (τ = 100 fs), EII is the dominating ionization channel, which favors the formation of maximum charged ions (Xe^{10+}, Xe^{11+}) in the cluster center. In contrast, BSI forms an inverse radial charge ordering with the highest charges in the exterior cluster shells. This suggests that the production of the two inverse radial charge distributions with an equal average ion charge can be forced by the choice of multiple pulses with different intensities and pulse lengths. At high intensities (10^{17}–10^{18} W cm^{-2}), where EII is insignificant and CE sets in much earlier, the BSI radial charge ordering and the enhancement of the ion charges beyond the single-atom limit by the ignition effect is observed only for short pulses.

PACS numbers: 36.40.Wa, 36.40.Gk, 71.15.Pd

DOI: 10.1134/S1054660X07050039

1. INTRODUCTION

Multielectron ionization of elemental and molecular clusters in ultraintense near-infrared laser fields (peak intensities $I_M = 10^{15}$–10^{18} W cm^{-2}, pulse durations 10–100 fs) is distinct from the electron dynamic response in ordinary fields, where perturbative quantum electrodynamics is applicable, and from the response of a single atomic and molecular species in terms of mechanisms, the ionization level, and the time scales for electron and nuclear dynamics [1–4]. Extreme multielectron cluster ionization involves three sequential–parallel processes of inner ionization, of nanoplasma formation and response, and of outer ionization [1–6]. Cluster electron dynamics triggers the nuclear dynamics of the Coulomb explosion [3, 4, 7–17]. Inner ionization, which is driven by barrier suppression ionization (BSI), is induced by a composite electric field involving the superposition of the laser field and the inner electric field of the nanoplasma ions and electrons. Extreme multielectron inner ionization of elemental rare-gas or molecular clusters containing heavy atoms, e.g., Xe_n [1–3] or $(HI)_n$ [17, 18], in ultraintense laser fields results in the production of extremely highly charged ions, e.g., Xe^{36+} from Xe_n clusters or I^{35+} from $(HI)_n$ clusters at $I_M = 10^{20}$ W cm^{-2} [17]. The nanoplasma consisting of the electrons and ions produced by inner ionization within the cluster induces an inner field that either enhances the inner ionization level (i.e., the "ignition effect") or retards it by the "screening effect" of the electrostatic interactions [2–4]. The nanoplasma electrons are driven by the laser field and induce electron impact ionizations (EII) within the cluster, which constitutes an additional channel for inner ionization. The nanoplasma electrons are removed from the cluster by outer ionization that is induced by the nanoplasma–laser interaction, with the outer ionization level determined by the laser intensity and pulse length [10]. The nanoplasma lifetime ranges from several hundreds of femtoseconds ("persistent nanoplasma") for large clusters and lower intensities of ~10^{15}–10^{16} W cm^{-2}, down to several tens of femtoseconds ("transient nanoplasma") for intensities of >10^{17} W cm^{-2}, depending on the outer ionization rate [10, 11, 19] and on dilution via the Coulomb explosion. These complex inner/outer ionization processes, nanoplasma response, and Coulomb explosion under the conditions of ultraintense laser-cluster interactions were explored by theoretical models [2–4, 6, 10, 19] and by computer simulations [3, 4, 6, 9, 10, 16, 19, 20].

The interrogation of dynamics at the temporal resolution of nuclear motion [21–23] and of electronic motion [24–27] raised important issues regarding the manipulations of the response and functionality of molecules and clusters through the use of shaped femtosecond and attosecond laser pulses. Different concepts and schemes were advanced for the control of dynamics on the time scale of nuclear motion, which rest on pump–dump control [28], coherent control [29], and control

by the use of tailored laser fields produced by pulse shaping [30–33] by the adaptation of closed-loop learning genetic algorithms [34, 35]. Control of electron dynamics was already accomplished by the use of single-cycle femtosecond laser pulses [24, 36–38] and attosecond laser pulses [39–41].

The traditional control methods of fs pulses from Ti:sapphire lasers (that are also utilized for the production of ultraintense pulses) are based on the shaping of the pulse train, amplitude, and phase. The use of conventional shaping devices for the tailoring of intense near-IR laser pulses is limited to the intensity range below $I_M \sim 10^{14}$ W cm^{-2} due to damage to the shapers [42, 43]. In this context, Zamith et al. [42] advanced and explored optimal control of the ionization level of Xe_n clusters by shaping the laser-pulse train at $I_M = 10^{14}$ W cm^{-2}, below the lowest limits of the ultraintense intensity domain of $I_M \geq 10^{15}$ W cm^{-2}. In this paper, we explore the control of ultraintense laser fields and study the control of extreme multielectron ionization levels in elemental Xe_n clusters in the intensity range $I_M = 10^{15}$–10^{18} W cm^{-2}. The control of reaction products in ultraintense laser fields is technically and conceptually different from the exploration of the control of ordinary fields. Ultraintense field control can be achieved by using different laser parameters—i.e., pulse intensity, temporal length, shape, phase, and train—in different experiments. Pulse shaping via learning algorithms is inapplicable under these experimental conditions; thus, an alternative way of changing the laser parameters is called for. Simulation methods recently developed for multielectron ionization and electron dynamics of clusters in ultraintense laser fields [42, 43] will provide guides for the experimental choice of laser pulses for optimal control. With these goals in mind, we shall utilize simulation results for multielectron ionization yields of Xe_n (2–2171) clusters at different laser pulse lengths and intensities to infer the perspectives for the control of inner ionization levels, i.e., to control the abundance and the spatial distribution of the ion charges.

2. METHODOLOGY

We advanced a molecular dynamics (MD) simulation scheme [1, 2, 8, 10, 20] for high-energy electron dynamics and nuclear dynamics in a cluster interacting with an electric and magnetic field of an ultraintense Gaussian laser pulse (peak intensities $I_M = 10^{15}$–10^{20} W cm^{-2}). The electron dynamics was treated relativistically, which is important in the highest intensity domain $I_M = 10^{18}$–10^{20} W cm^{-2}. The laser electric and magnetic fields were taken as

$$F_1(t) = F_M \exp[-2.773t^2/\tau^2]\cos(2\pi\nu t), \quad (1)$$

$$B_1(t) = B_M \exp[-2.773t^2/\tau^2]\cos(2\pi\nu t), \quad (2)$$

with $F_M = 2.745 \times 10^{-7}\ I_M^{1/2}$ (F_M given in eV Å^{-1} and I_M in W cm^{-2}) and $B_M = 9.155 \times 10^{-11}\ I_M^{1/2}$ (B_M given in eV Å^{-2} fs). For the laser parameters, we used $\nu = 0.35$ fs^{-1} (photon energy 1.44 eV) and a pulse temporal length (FWHM) $\tau = 10$–100 fs. The peak of the laser pulse is attained at $t = 0$. An initially truncated laser pulse was used, with the (negative) initial time t_s, at which the laser electric field reaches the critical threshold value for the first ionization of Xe by the classical barrier suppression ionization (BSI) mechanism [1, 2], neglecting tunnel ionization. Accordingly, the initial plasma setup for the MD simulations consists of all xenon atoms being singly ionized and the corresponding electrons being placed at the classical BSI barriers. The critical electric field strength F for the $Xe^{q+} \longrightarrow Xe^{(q+1)+} + e$ ionization is

$$F = \frac{P_{q+1}^2}{4\bar{B}(q+1)q_e^2}, \quad (3)$$

with the ionization potential P_{q+1}, the electron charge $q_e = -1$, q for the charge of the initial ion or atom (prior to ionization), and $\bar{B} = 14.40$ eV Å. The position vector of the barrier location relative to the parent ion is

$$\mathbf{r}_b = \left(\frac{\bar{B}(q+1)}{F^3}\right)^{1/2}\mathbf{F}, \quad (4)$$

with $F = |\mathbf{F}|$. The initial threshold field $F_{th} = F$ for the first ionization is obtained from Eq. (3), with $q = 0$. At every MD step, the possibility of BSI is checked for, inquiring at each ion whether the sum of the inner electric fields of all other ions and electrons and the external electric laser field exceeds the critical field strength, Eq. (3), for the next ionization. In our simulations, we have also included single EII processes $Xe^{q+} + e \longrightarrow Xe^{(q+1)+} + 2e$, using experimental data for the cross sections, which are available up to $q = 10$ [44]. The ion–ion, ion–electron, and electron–electron interactions were described by the Coulomb potentials, the ion–electron and electron–electron potentials were smoothed for short distances to improve the energy conservation of the MD simulations [2].

3. RESULTS AND DISCUSSION

Figure 1 presents an overview of the average ionization level $n_{ii}^L \equiv n_{ii}(t_L)$ (i.e., the average charge per ion at long time t_L at the end of the trajectories) accessible for Xe_n ($n = 55$–2171) clusters over the intensity range $I_M = 10^{15}$–10^{20} W cm^{-2} and for a pulse length of $\tau = 25$ fs. The average ionization level ranges from $n_{ii}^L = 5.5$ at $I_M = 10^{15}$ W cm^{-2} to $n_{ii}^L = 36$ at $I_M = 10^{20}$ W cm^{-2}. For comparison, the atomic limits of n_{ii}^L obtained for

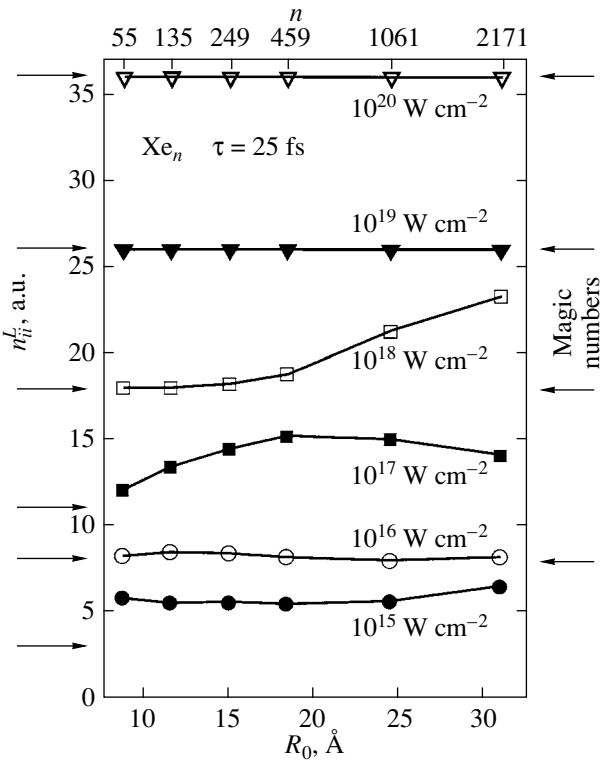

Fig. 1. The cluster size and laser intensity dependence of the average inner ionization level n_{ii}^L at long times for Xe_n clusters (n = 55–2171) in the intensity range $I_M = 10^{15}$–10^{20} W cm^{-2} (marked at the curves) with a laser pulse length of τ = 25 fs. The horizontal arrows marked "atomic limit" represent the single-atom ionization level calculated from the BSI model. The horizontal arrows on the right-hand side marked "magic numbers" are the charges which correspond to electronic shell closures of the xenon atom.

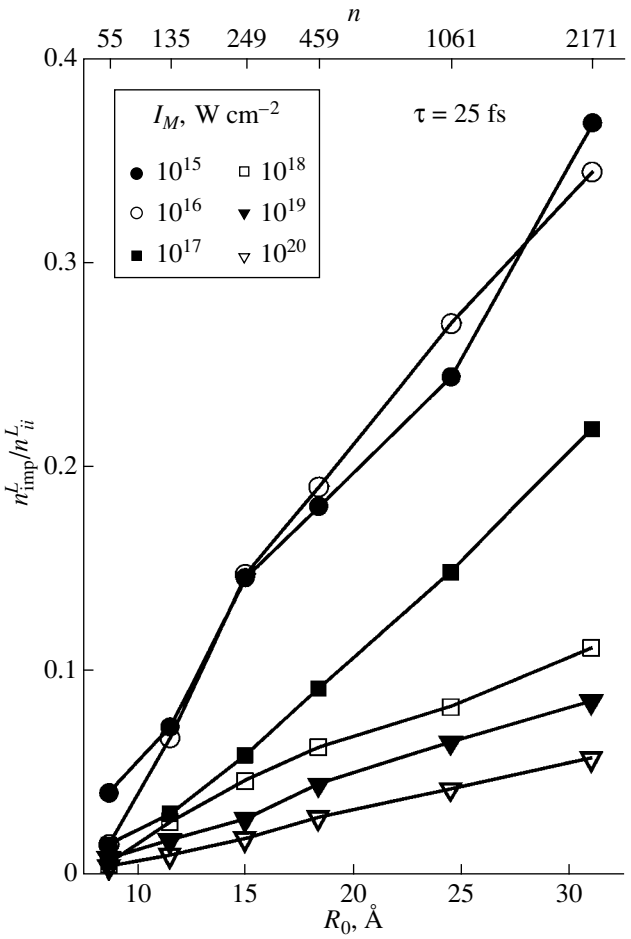

Fig. 2. The cluster size dependence of the relative EII yield n_{imp}^L/n_{ii}^L for Xe_n (n = 55–2171) clusters in the intensity range $I_M = 10^{15}$–10^{20} W cm^{-2} and a pulse length of τ = 25 fs.

the external laser electric field by the classical BSI critical field strength formula, Eq. (3), are also included in Fig. 1. For the intensities 10^{15} and 10^{17}–10^{20} W cm^{-2}, the atomic limits Xe^{8+}, Xe^{18+}, Xe^{26+}, and Xe^{36+} coincide with the electronic shell closures of xenon ("magic numbers"). For 10^{17} and 10^{18} W cm^{-2}, n_{ii}^L shows a pronounced cluster size dependence, while for 10^{19} and 10^{20} W cm^{-2}, the n_{ii}^L level is constant, corresponding to the atomic limit. For 10^{15} and 10^{16} W cm^{-2}, a weak cluster size dependence is observed with a marked deviation from the atomic limit at 10^{15} W cm^{-2}. Figure 2 shows the cluster size and laser intensity dependence of the relative EII yield n_{imp}^L/n_{ii}^L for a pulse length of 25 fs, where n_{imp}^L is the average number of impact ionizations per atom at long times. The relative EII yield increases with an increasing cluster size and decreasing laser intensity. For low intensities 10^{15}–10^{16} W cm^{-2} and large clusters (Xe_{2171}), the relative EII yield approaches 40% and is an important ionization channel.

Further insight into the inner ionization process and yields is obtained from Fig. 3, where the n_{ii}^L values together with their BSI and EII contributions, n_{BSI}^L and n_{imp}^L ($n_{ii}^L = n_{BSI}^L + n_{imp}^L$), as well as the maximum ion charge q_{max}, are given as a function of the cluster size in the intensity range 10^{15}–10^{18} W cm^{-2} and a pulse length of τ = 25 fs. Two sets of n_{ii}^L values are presented in Fig. 3. The total values of n_{ii}^L include the contributions of both BSI and EII (indicated by filled circles) which correspond to the data given in Figs. 1 and 2. A second set of values marked as "n_{ii}^L (without EII)" was obtained from a simulation series in which the EII channel was switched off (indicated by open circles). From Fig. 3, we conclude:

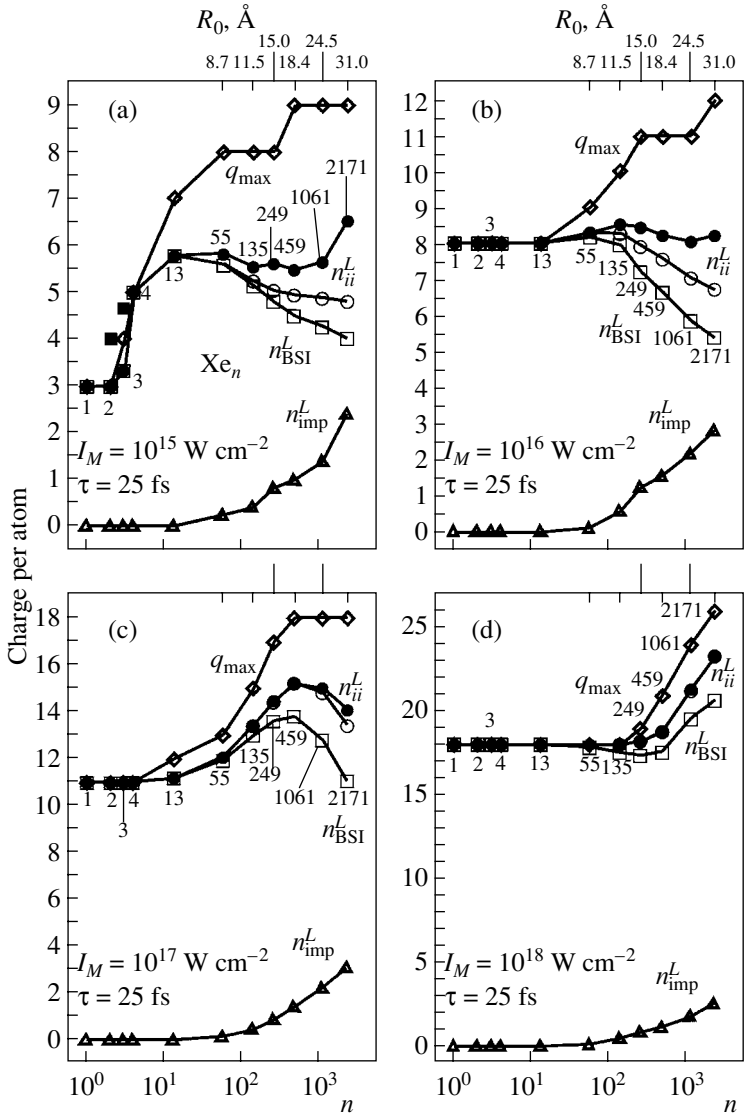

Fig. 3. The cluster size dependence of long time BSI level n_{BSI}^L (□), the EII level n_{imp}^L (△), the total inner ionization level $n_{ii}^L = n_{BSI}^L + n_{imp}^L$ (●), the n_{ii}^L (without EII) values (○), and the maximal ionic charge q_{max} (◇) for Xe$_n$ (n = 1–2171) clusters. (a) $I_M = 10^{15}$ W cm^{-2}, τ = 25 fs. For Xe_2 and Xe_3, the $n_{ii}^L = n_{BSI}^L$ values strongly depend on the orientation of the cluster in the external laser electric field, manifesting an extreme ignition effect. For a parallel orientation of the (long) molecular axis, the n_{ii}^L values are 4.0 and 4.7 for Xe_2 and Xe_3, respectively (■), while for a perpendicular orientation the corresponding values are 3.0 and 3.3, respectively (●). (b) $I_M = 10^{16}$ W cm^{-2}, τ = 25 fs. (c) $I_M = 10^{17}$ W cm^{-2}, τ = 25 fs. (d) $I_M = 10^{18}$ W cm^{-2}, τ = 25 fs.

(1) Over the entire intensity range of 10^{15}–10^{18} W cm^{-2}, the maximum ion charge q_{max} and the number of impact ionizations n_{imp}^L per atom increase monotonously with increasing the cluster size n.

(2) The n_{ii}^L (without EII) values are higher than the corresponding n_{BSI}^L values for the same cluster size and laser intensity. Correspondingly, the differences between the two n_{ii}^L sets, $\Delta n_{ii}^L = n_{ii}^L - n_{ii}^L$ (without EII), are lower than the corresponding n_{imp}^L values. This means that Δn_{ii}^L represents the net EII enhancement, while the rest, $n_{imp}^L - \Delta n_{ii}^L = n_{ii}^L$ (without EII) – n_{BSI}^L, accounts for the competition between the two ionization channels, reflecting the kinetics of the two ionization mechanisms. The net effect of the EII Δn_{ii}^L decreases with increasing the laser intensity. For Xe_{2171}, the EII net enhancement Δn_{ii}^L is 1.74, 1.52, 0.68, and ≈0

for 10^{15}, 10^{16}, 10^{17}, and 10^{18} W cm^{-2}, respectively, while the corresponding n_{imp}^{L} values are 2.40, 2.83, 3.08, and 2.59.

(3) Both ignition and screening effects are known to increase with increasing cluster size [1, 10], although their effect on n_{ii}^{L} is of opposite signs, while the attainment of the single-atom value of n_{ii}^{L} indicates their complete cancellation (or their absence). Since the n_{ii}^{L} (without EII) values (open circles) are not affected by the competing EII channel, they provide information about the interplay between ignition and screening effects. For 10^{15} W cm^{-2}, the n_{ii}^{L} (without EII) values decrease for cluster sizes $n > 55$, although still being higher than the single-atom value. This means that the ignition effect predominates over the entire cluster size domain, although its influence is increasingly weakened with increasing cluster size. At 10^{16} W cm^{-2}, the ignition effect prevails only for Xe_{55} and Xe_{135}, while for larger clusters the screening effect increasingly predominates. At 10^{17} W cm^{-2}, the ignition effect prevails over the entire cluster size range, but its influence decreases for $n \geq 1061$. At 10^{18} W cm^{-2}, the ignition effect is dominating for all cluster sizes and increases with increasing cluster size.

(4) The steep increase of the n_{ii}^{L} level from 3.0 to 5.8 at 10^{15} W cm^{-2} for small clusters $1 \leq n \leq 13$ represents an extreme example of the ignition effect and is the reason for the nonconvergence of the n_{ii}^{L} values for 10^{15} W cm^{-2} to the single-atom limit in Fig. 1 [20]. For Xe_2 and Xe_3, the ignition effect also depends on the spatial orientation of the cluster; the parallel orientation of the cluster with respect to the external laser electric field leads to higher n_{ii}^{L} values (filled squares) than the perpendicular orientation (filled circles). For higher laser intensities, the ignition effect is of no consequence in the small cluster size domain, since its contribution to the total electric field is comparatively small. A minor exception is the nonconvergence of the n_{ii}^{L} level for Xe_{55} to the single-atom value at 10^{17} W cm^{-2} (Fig. 1).

(5) The net contribution of EII to n_{ii}^{L} is important at 10^{15} and 10^{16} W cm^{-2}, overcompensating or at least compensating, for the screening effect, which would otherwise lead to a decrease of n_{ii}^{L} with increasing cluster size.

The cluster size dependence of n_{ii}^{L}, and of its contributions n_{BSI}^{L} and n_{imp}^{L}, indirectly indicates controllability of these quantities by the laser parameters, since the same effects which are responsible for the cluster size dependence are also manifested in the time-dependent nanoplasma density and composition. Therefore, controllability can be expected from the timing of the laser pulse (i.e., the choice of pulse lengths and shapes) with the depletion of the nanoplasma electrons by outer ionization and by the Coulomb explosion, which define the clock of these systems. According to the cluster size dependence of the ionization levels, controllability may be expected in the intensity range 10^{15}–10^{18} W cm^{-2}, unlike for 10^{19}–10^{20} W cm^{-2}, where n_{ii}^{L} remains constant at the atomic limit over the entire cluster size domain (Fig. 1).

Figure 4 shows the pulse length dependence of n_{ii}^{L}, n_{ii}^{L} (without EII), n_{BSI}^{L} and n_{imp}^{L} for laser intensities 10^{15}–10^{18} W cm^{-2}. At 10^{15} W cm^{-2}, the average ionization level n_{ii}^{L} increases markedly with an increasing pulse length. The increase of n_{ii}^{L} from 6.53 to 9.30 by 2.77 with an increasing pulse length from 25 to 100 fs is reflected by the increase of 2.80 for n_{imp}^{L}, while, concurrently, the n_{BSI}^{L} values remain independent of τ. The stagnation of the BSI is partly due to competition with the EII channel; as the n_{ii}^{L} (without EII) values exhibit a moderate increase of 1.67 for the same pulse lengths. At 10^{16} W cm^{-2}, the increase of n_{ii}^{L} with an increasing pulse length is less pronounced and, unlike for 10^{15} W cm^{-2}, levels off for long pulses. Again, the increase of n_{ii}^{L} is reflected by the n_{imp}^{L} values, while the n_{BSI}^{L} values stagnate. The n_{ii}^{L} values are higher than the n_{ii}^{L} (without EII) values, but their increase by 1.37, when extending the pulse length from 25 to 100 fs, is smaller than by 1.98 for n_{ii}^{L} (without EII). The larger increase of the n_{ii}^{L} (without EII) values may be due to the smaller number of nanoplasma electrons and the resulting smaller screening. The pulse length dependence of the average ionization levels at 10^{17} and 10^{18} W cm^{-2} is qualitatively different from that at lower intensities. Not only is EII of minor importance at $I_M = 10^{17}$ and 10^{18} W cm^{-2}, the n_{ii}^{L} and n_{BSI}^{L} values decrease monotonously or pass a maximum and then decrease with increasing pulse length. This qualitatively different behavior is due to the faster Coulomb explosion, which increases the interatomic distances before the external laser field reaches its maximum. Accordingly, ignition has no effect on n_{ii}^{L} at 10^{18} W cm^{-2} and $\tau = 100$ fs, where n_{ii}^{L} is reduced to the single-atom value of 18.

Figure 5 presents the spatial distributions $n(q, r)$ of the Xe^{q+} ions at distances r from the center of the Xe_{2171}

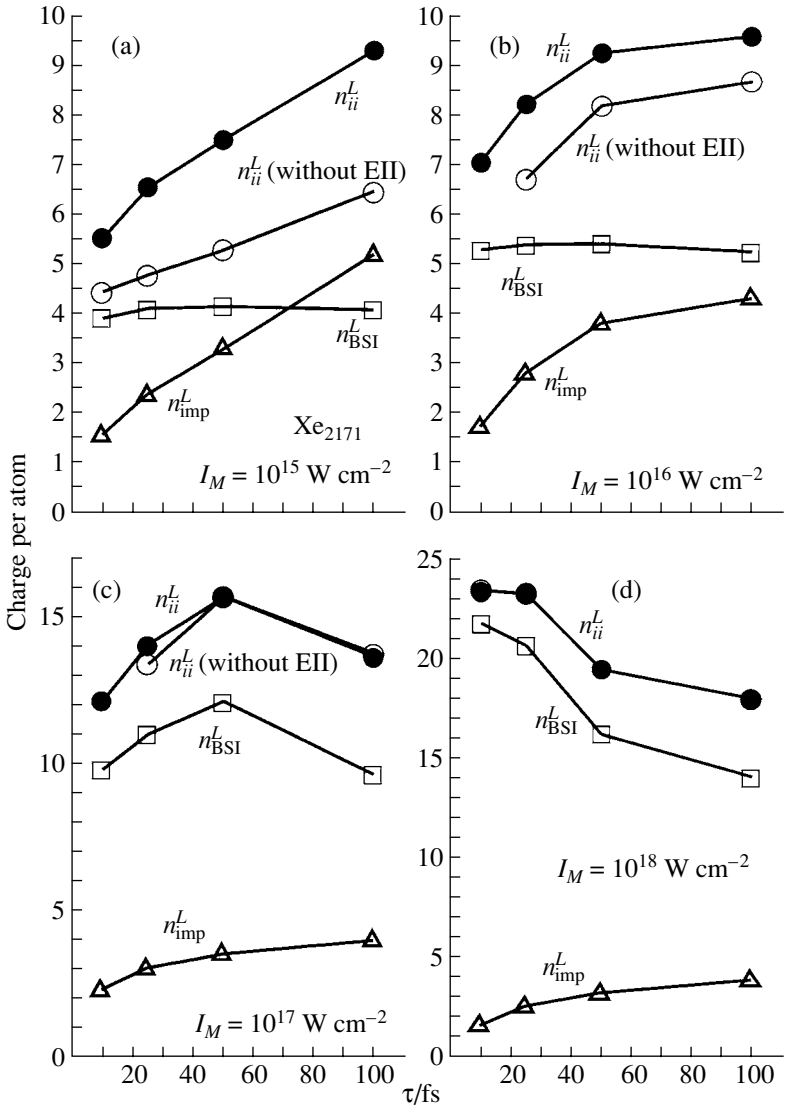

Fig. 4. The pulse length dependence of the long time inner ionization levels for Xe_{2171} and intensities $I_M = 10^{15}$–10^{18} W cm^{-2}. Ionization levels are presented for n_{BSI}^L (□), n_{imp}^L (△), $n_{ii}^L = n_{\mathrm{BSI}}^L + n_{\mathrm{imp}}^L$ (●), and n_{ii}^L (without EII) (○).

cluster at long times t_L, which mark the end of the trajectories. The spatial distribution was presented for intervals of $\Delta r = R(t_L)/20$, with the cluster radius $R(t_L)$ at that time. In this way, distribution functions for different intensities and pulse lengths can be better compared, avoiding the dependence of $R(t_L)$ on the choice of the trajectory length $t_L - t_s$. $n(q, r)$ obeys the normalization condition $\sum_q \sum_r n(q, r)\Delta r = 1$. The spatial distributions are given for $\tau = 10$, 25, 50, and 100 fs and $I_M = 10^{15}$, 10^{16}, 10^{17}, and 10^{18} W cm^{-2}.

For $I_M = 10^{15}$ W cm^{-2} and pulse lengths of $\tau = 10$ and 25 fs (Fig. 5a), the maximum charges (q = 7–9) are found in the exterior cluster shells. Such ion charge distributions are characteristic for the ignition effect, by which the highest local fields are generated in the cluster periphery. At $\tau = 100$ fs, the maximum ion charges rise to $q = 10$ and 11, being exclusively generated by EII. EII becomes the predominating ionization channel with $n_{\mathrm{imp}}^L / n_{ii}^L = 0.56$. Remarkably, the charge distribution is inverted with the highest ion charges being found in the center of the cluster. Since BSI is predominant for short pulses and favors highly charged ions in the cluster periphery, while EII becomes important for long pulses and favors ions in the cluster center, this opens up possibilities for the control of the ion charge distribution. The distribution $n(q, r)$ for $\tau = 50$ fs (third panel of Fig. 5a) represents an intermediate case; the majority of maximum charged ions is already found in the cluster center, but the maximum charge is still 9.

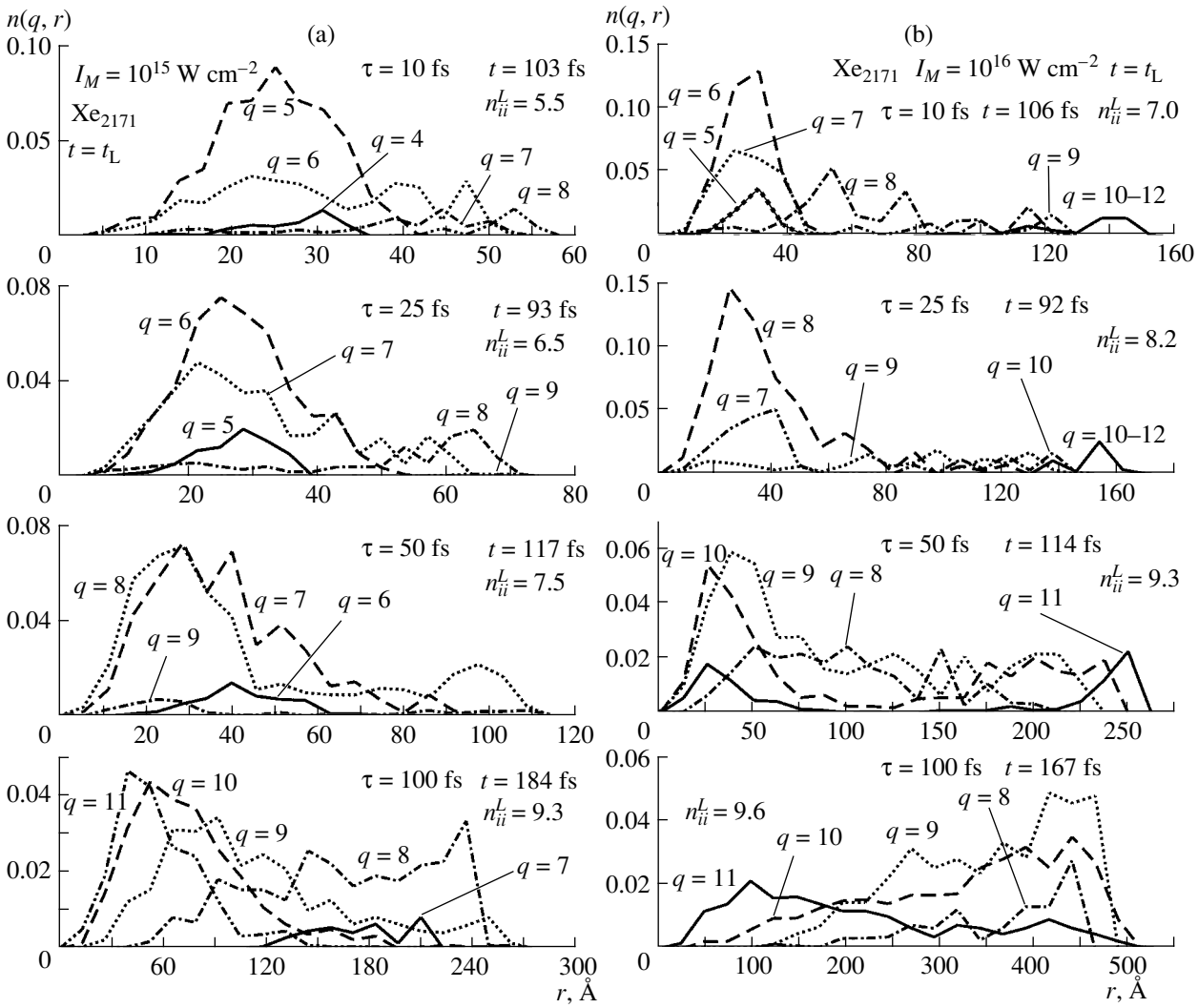

Fig. 5. The radial distribution functions $n(q, r)$ of Xe^{q+} ions at long times t_L (end of the trajectories) for Xe_{2171} in the intensity range $I_M = 10^{15}$–10^{18} W cm^{-2} and for pulse lengths of $\tau = 10$, 25, 50, and 100 fs. $n(q, r)$ satisfies the normalization condition $\sum_q \sum_r n(q, r)\Delta r = 1$ and is given at regular distance intervals $\Delta r = R(t_L)/20$ from the cluster center, with $R(t_L)$ being the cluster radius at $t = t_L$. The pulse lengths τ, the times $t = t_L$, and the average ionization levels n_{ii}^L are labeled on each panel. (a) $I_M = 10^{15}$, (b) 10^{16}, (c) 10^{17}, and (d) 10^{18} W cm^{-2}.

The situation at $I_M = 10^{16}$ W cm^{-2} (Fig. 5b) is similar. For short pulse lengths, $\tau = 10$ and 25 fs, the ion charge distributions exhibit maximum charges in the cluster periphery and, thus, manifest the predominance of BSI, while for $\tau = 100$ fs, the charge distribution is inverted, with the maximum charges in the cluster center, and reflects the signature of EII, although not as pronounced as for the same pulse length at 10^{15} W cm^{-2} (Fig. 5a). The case of $I_M = 10^{16}$ W cm^{-2}, $\tau = 50$ fs (third panel of Fig. 5b) again represents an intermediate case, showing, by its bimodal distribution of the highest ion charges ($q = 10$, 11), the influence of both ionization channels. Unlike 10^{15} W cm^{-2}, at the higher intensity of 10^{16} W cm^{-2}, Xe^{10+} and Xe^{11+} ions are formed by both ionization channels. Interestingly, these laser parameters lead to the same average ion charge of 9.30 as the pulse parameters $I_M = 10^{15}$ W cm^{-2} and $\tau = 100$ fs (lowest panel of Fig. 5a), but with a different ion charge distribution. Thus, the two sets of pulse parameters ($I_M = 10^{15}$ W cm^{-2}, $\tau = 100$ fs and $I_M = 10^{16}$ W cm^{-2}, $\tau = 50$ fs) provide an example of the aforementioned controllability concept of influencing the ion charge distribution by selecting the ionization channel via the pulse parameters.

At $I_M = 10^{17}$ W cm^{-2} and $\tau = 10$ and 25 fs (two uppermost panels of Fig. 5c), $n(q, r)$ exhibits the characteris-

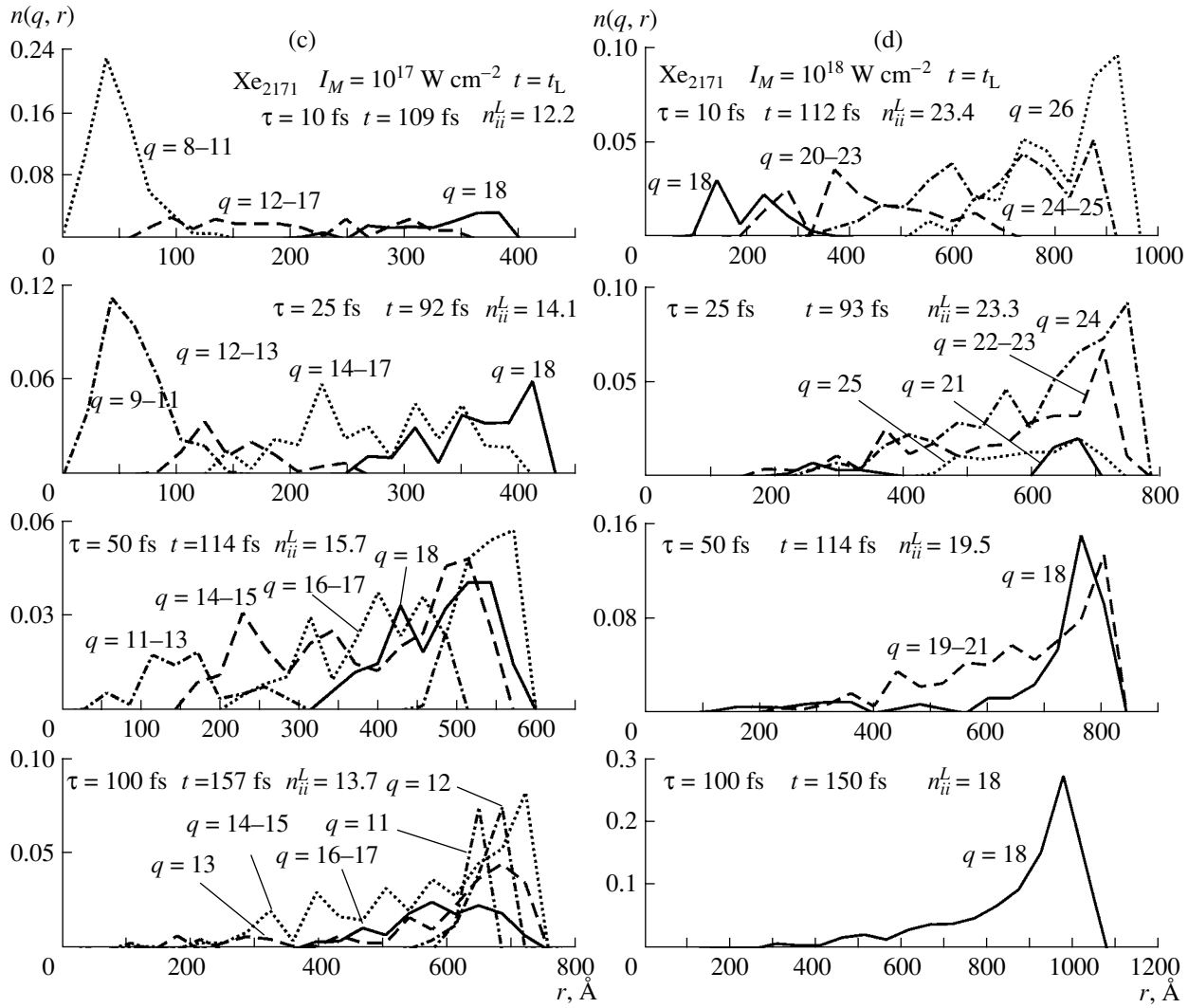

Fig. 5. (Contd.)

tic BSI charge ordering, i.e, increasing ion charges with increasing distance from the center of the cluster. However, the charge ordering is not preserved for longer pulses, where the distributions of different charges excessively overlap. Since the ion charges involved are in the range 11–18, transcending the maximum EII level implemented in our simulations, EII can be ruled out as a cause for the breakdown of the charge ordering. Rather, the Coulomb explosion, which is also responsible for the decrease of the average ion charge at τ = 100 fs, is the underlying mechanism for the qualitative change of the charge distribution functions. Apparently, in the case of the 100-fs pulse (lowermost panel of Fig. 5c), the outer ion shell expands into space before the external field and ignition effect can lead to highly charged ions. Only inner cluster shells, whose expansion in space is slower, experience a sufficient ignition effect, which, however, in the case of a 100-fs pulse, is not anymore intense enough to form Xe^{18+} ions. The formation of Xe^{18+} ions requires a slower Coulomb explosion, which is still realized for the 50-fs pulse (third panel of Fig. 5c). In conclusion, the overlapping charge distribution functions obtained for longer pulse lengths imply the notion of a (not necessarily spherical) zone inside the cluster, in which the ignition effect still supports the formation of ions higher than the single-atom limit. With increasing time, i.e., with the advancement of the Coulomb explosion, this zone moves towards the center of the cluster.

At 10^{18} W cm^{-2} (Fig. 5d), the situation is very similar to that at 10^{17} W cm^{-2}, although more pronounced due to the faster Coulomb explosion. For τ = 10 fs (uppermost panel of Fig. 5a), a maximum ion charge of q = 26 is observed with the characteristic BSI spatial charge ordering, i.e., the highest ion charges in the cluster periphery and the lowest charges in the center of the cluster. For τ = 25 fs (second panel of Fig. 5d), the charge ordering is already eroded for the most part. The

maximum ion charge drops to 25 and moves inward the cluster. This trend is continued for $\tau = 50$ fs, where the erosion of spatial ordering is complete and a large number of ions assume the single-atomic limit of $q = 18$. At $\tau = 100$ fs, the ignition effect is no longer strong enough to boost the ion charges beyond the single-atomic level.

4. CONCLUSIONS

Our results provide the conceptual framework for laser control of the ionization levels of elemental Xe_n clusters in ultraintense laser fields. Of course, the ionization levels markedly increase with rising laser intensity, but this constitutes a trivial mode of control. A significant mode of control involves the product change (i.e., the ionization levels and the spatial distributions of ions) at a fixed laser intensity, which is induced by changing the pulse parameters, e.g., the pulse length. Our results predict a marked dependence of the ionization and the ions' spatial distributions on the temporal laser pulse length and elucidate the relevant mechanisms over a broad intensity domain.

In the lower intensity domain of $I_M = 10^{15}$–10^{16} W cm^{-2}, BSI is important for short pulses, while EII makes a significant contribution for longer pulses. The controllability concept for large clusters in this lower intensity domain involves the increase of the ionization level (while markedly affecting the charge distribution) by increasing the pulse length. It might be possible to force the inversion of the charge distribution (i.e., the highest charges in the cluster interior) by a sequence of two pulses; a first short pulse which produces enough nanoplasma electrons and a second long but weaker pulse, which is sufficiently strong to drive the nanoplasma electrons for inducing impact ionizations, but weak enough to avoid BSI. These results in the lower intensity domain of $I_M = 10^{15}$–10^{16} W cm^{-2} established a laser control mechanism driven by BSI and by EII of the persistent nanoplasma. Furthermore, the effects of the cluster Coulomb explosion on the ionization level for different pulse lengths are not significant.

In the high intensity domain of $I_M = 10^{17}$–10^{18} W cm^{-2} studied herein, the nanoplasma is transient and the contribution of the EII mechanism is minor, while the BSI mechanism is dominant. In this intensity range, the erosion of the spatial charge ordering is manifested with increasing pulse lengths due to the effects of the Coulomb explosion. In the high intensity range, the average cluster ionization level decreases with an increasing pulse length, manifesting the decrease of the ignition effect on BSI due to the spatial expansion of the cluster.

The strategies for control in ultraintense laser fields are quite distinct from the traditional approach to laser control through the tailoring of laser pulses [34]. Another example for such novel phenomena pertains to branching ratios in nucleosynthesis [45]. The Coulomb explosion of extremely ionized molecular heteroclusters containing carbon, deuterium, and hydrogen will result in branching between $^{12}C(p, \gamma)^{13}N$ nucleosynthesis and the $^{2}D(d, n)^{3}He$ dd fusion [45]. To be more explicit, consider the Coulomb explosion of a completely ionized $(CH_3D)_n$ cluster:

$$(CH_3D)_n \longrightarrow C^{6+} + D^+ + 3H^+.$$

Two parallel nuclear reactions are expected to occur in the nanoplasma filament:

$$^{12}C^{6+} + {}^{1}H^+ \longrightarrow {}^{13}N^{7+} + \gamma; \quad {}^{12}C(p, \gamma)^{13}N,$$

$$^{2}D^+ {}^{2}D^+ \longrightarrow {}^{3}He^{2+} + n; \quad {}^{2}D(d, n)^{3}He.$$

Control of the branching ratios between these two reactions (interrogated by monitoring the ratio of the numbers of (γ rays)/(neutrons)) can be induced by changing the cluster size and the laser parameters. Lowering the laser intensity in the threshold region for complete C atom ionization can reduce the contribution of the $^{12}C(p, \gamma)^{13}N$ reaction, while changing the pulse shape may modify the energetics of the Coulomb explosion.

ACKNOWLEDGMENTS

This research was supported by the Deutsche Forschungsgemeinschaft (DFG) SFB 450 on the "Analysis and Control of Ultrafast Photoinduced Reactions," and by the James Franck Binational German-Israeli Program on Laser–Matter Interaction.

REFERENCES

1. I. Last and J. Jortner, Phys. Rev. A **62**, 013201 (2000).
2. I. Last and J. Jortner, J. Chem. Phys. **120**, 1336 (2004).
3. U. Saalmann, Ch. Siedschlag, and J. M. Rost, J. Phys. B **39**, R39 (2006).
4. V. P. Krainov and M.B. Smirnov, Phys. Rep. **370**, 237 (2002).
5. I. Last and J. Jortner, J. Chem. Phys. **120**, 1348 (2004).
6. I. Last and J. Jortner, Phys. Rev. A **71**, 013022 (2006).
7. Ch. Siedschlag and J.M. Rost, Phys. Rev. A **71**, 031401(R) (2005).
8. I. Last and J. Jortner, Phys. Rev. Lett. **87**, 033401 (2001).
9. I. Last and J. Jortner, J. Phys. Chem. A **106**, 10877 (2002).
10. I. Last and J. Jortner, J. Chem. Phys. **121**, 3030 (2004).
11. I. Last and J. Jortner, J. Chem. Phys. **121**, 8329 (2004).
12. J. Zweiback, T. E. Cowan, R. A. Smith, et al., Phys. Rev. Lett. **85**, 3640 (2000).
13. J. Zweiback, T. E. Cowan, J. H. Hartley, et al., Phys. Plasma **9**, 3108 (2002).
14. K. W. Madison, P. K. Patel, M. Allen, et al., Phys. Rev A **70**, 053201 (2004).
15. G. Grillon, Ph. Balcou, J.-P. Chambaret, et al., Phys. Rev. Lett. **89**, 065005 (2002).
16. S. Ter-Avertisyan, M. Schnürer, D. Hilscher, et al., Phys. Plasmas **12**, 012702 (2005).
17. A. Heidenreich, I. Last, and J. Jortner, Proc. Natl. Acad. Sci. USA **103**, 10589 (2006).

18. I. Last and J. Jortner, Phys. Rev. A **71**, 063204 (2005).
19. A. Heidenreich, I. Last, and J. Jortner, Isr. J. Chem. (in press).
20. A. Heidenreich, I. Last, and J. Jortner, submitted to J. Chem. Phys. (2006).
21. S. A. Rice and M. Zhao, *Optical Control of Molecular Dynamics* (Wiley, New York, 2000).
22. M. Shapiro and M. Brumer, *Principles of Quantum Control of Molecular Processes* (Wiley, Hoboken, N.J., 2003).
23. D. J. Tannor, *Introduction to Quantum Mechanics: A Time-Dependent* Perspective (University Science Books, Sausalito, 2006).
24. T. Brabec and F. Krausz, Rev. Mod. Phys. **72**, 545 (2000).
25. P. B. Corkum, Phys. Rev. Lett. **71**, 1994 (1993).
26. V. R. Bhardwaj, P. B. Corkum, and D. M. Raner, Phys. Rev. Lett. **93**, 43001 (2004).
27. E. Eremina, X. Liu, H. Rottke, et al., Phys. Rev. Lett. **92**, 173001 (2004).
28. D. J. Tannor and S. A. Rice, J. Chem. Phys. **83**, 5013 (1985).
29. P. Brumer and M. Shapiro, Faraday Discuss. Chem. Soc. **82**, 177 (1986).
30. A. P. Peirce, M. A. Dahleh, and H. Rabitz, Phys. Rev. A **37**, 4950 (1988).
31. S. Shi and H. Rabitz, Chem. Phys. **139**, 185 (1989).
32. R.S. Judson and H. Rabitz, Phys. Rev. Lett. **68**, 1500 (1992).
33. W.S. Warren, H. Rabitz, and M. Dahleh, Science **259**, 1581 (1993).
34. S. Vajda, P. Rosendo-Francisco, C. Kaposta, et al., Eur. Phys. J. D **16**, 161 (2001).
35. T. Brixner, N.H. Damrauer, P. Niklaus, and G. Gerber, Nature **414**, 57 (2001).
36. G. G. Paulus, F. Lindner, H. Walther, et al., Phys. Rev. Lett. **91**, 253004 (2003).
37. X. Liu, H. Rottke, E. Eremina, et al., Phys. Rev. Lett. **93**, 263001 (2004).
38. C. C. Chirila and R. M. Potvliege, Phys. Rev. A **71**, 021402 (2005).
39. M. Hentschel, R. Kienberger, Ch. Spielmann, et al., Nature **414**, 509 (2001).
40. M. Kitzler, K. O'Keefe, and M. Lezius, J. Mod. Opt. **53**, 57 (2006).
41. A. Fohlisch, P. Feulner, F. Hennies, et al., Nature **436**, 373 (2005).
42. S. Zamith, T. Martchenko, Y. Ni, et al., Phys. Rev. A **70**, 011201(R) (2004).
43. T. Martchenko, Ch. Siedschlag, S. Zamith, et al., Phys. Rev. A **72**, 53202 (2005).
44. A. Heidenreich, I. Last, and J. Jortner, Eur. Phys. J. D **35**, 567 (2005).
45. I. Last and J. Jortner, Pys. Rev. Lett. **97**, 173401 (2006).